scientific reports

OPEN

Two-stage variable-fidelity modeling of antennas with domain confinement

Anna Pietrenko-Dabrowska[1,2]✉, Slawomir Koziel[1,2] & Lukasz Golunski[1]

Surrogate modeling has become the method of choice in solving an increasing number of antenna design tasks, especially those involving expensive full-wave electromagnetic (EM) simulations. Notwithstanding, the curse of dimensionality considerably affects conventional metamodeling methods, and their capability to efficiently handle nonlinear antenna characteristics over broad ranges of the system parameters is limited. Performance-driven (or constrained) modeling frameworks may be employed to mitigate these issues by considering a construction of surrogates from the standpoint of the antenna performance figures rather than directly geometry parameters. This permits a significant reduction of the model setup cost without restricting its design utility. This paper proposes a novel modeling framework, which capitalizes on the domain confinement concepts and also incorporates variable-fidelity EM simulations, both at the surrogate domain definition stage, and when rendering the final surrogate. The latter employs co-kriging as a method of blending simulation data of different fidelities. The presented approach has been validated using three microstrip antennas, and demonstrated to yield reliable models at remarkably low CPU costs, as compared to both conventional and performance-driven modeling procedures.

Design of contemporary antenna structures is to a large degree based on full-wave electromagnetic (EM) simulation models[1–4], which are used for the development of antenna topology[5], parametric studies[6], as well as geometry adjustment[7,8]. The need for EM analysis arises from the fact that alternative representations (e.g. parameterized equivalent networks) are either non-reliable or non-existent. Moreover, EM simulations reliably account for mutual coupling, the effects of housing, connectors, etc. Furthermore, antenna structures become increasingly sophisticated to realize the assumed functionalities (multi-band and MIMO operation, circular polarization, etc.)[9–13]. To enable these, a variety of topological alterations are incorporated (stubs, defected grounds structures and so on)[14–17], all of which have to be properly dimensioned. EM analysis is CPU intensive, which impedes execution of EM-driven procedures that entail repetitive simulations, such as optimization[18], statistical analysis[19,20], design centering[21,22], let alone global[23] or multi-objective search[24], especially for complex devices[25–27].

Accelerating EM-based procedures is a matter of practical necessity. Numerous techniques have been developed for that purpose. In the realm of local optimization, we have adjoint sensitivities[28], mesh deformation[29], selective gradient updates[30,31], or the employment of customized EM solvers[32]. In a broader context, surrogate-assisted approaches has been growing in popularity, both concerning physics-based models (space[33] or manifold mapping[34], shape-preserving response prediction[35], or adaptive response scaling[36]), and data-driven ones, e.g. kriging[37], artificial neural networks (ANN)[38], radial-basis functions (RBF)[39], support vector regression (SVR)[40], Gaussian process regression (GPR)[41], or polynomial chaos expansion[42]. The latter are frequently used in global and multi-criterial optimization[43–45]. Among other noteworthy methods feature-based optimization (FBO)[46–48] and cognition-based design[49], in which the design task is re-mapped into the space of adequately pinpointed attributes (points) of the system outputs, the latter being in weakly nonlinear relationship with the geometry parameters.

Needless to say, replacing EM analysis by fast surrogates is invaluable as an acceleration tool. Approximation models (kriging[50], RBF[51], PCE[52], SVR[53], ANNs and numerable variants thereof, e.g. convolutional neural networks (CNN)[54] or deep neural networks (DNN)[55]) are particularly popular due to their accessibility[56,57]. However, data-driven modeling methodologies are largely influenced by the curse of dimensionality and at the same time, have limited capability to represent highly nonlinear antenna characteristics. Available mitigation tools, e.g. least-angle regression (LAR)[58], high-dimensional model representation (HDMR)[59], are not suitable

[1]Faculty of Electronics, Telecommunications and Informatics, Gdansk University of Technology, 80-233 Gdansk, Poland. [2]Present address: Engineering Optimization & Modeling Center, Reykjavik University, 102 Reykjavik, Iceland. ✉email: anna.dabrowska@pg.edu.pl

Description	Notation
Antenna parameter vector	$\boldsymbol{x} = [x_1 \ldots x_n]^T$
Conventional parameter space	$X = [\boldsymbol{l}, \boldsymbol{u}]$
Lower bounds on the parameters	$\boldsymbol{l} = [l_1 \ldots, l_n]^T$
Upper bounds on the parameters	$\boldsymbol{u} = [u_1 \ldots, u_n]^T$
Figures of interest	f_k, $k = 1, \ldots, N$
Objective space	F: $f_{k.\min} \le f_k^{(j)} \le f_{k.\max}$, $k = 1, \ldots, N$
Objective vector	$\boldsymbol{f} = [f_1 \ldots f_N]^T$

Table 1. Notation used in performance-driven modeling.

for general-purpose antenna modeling. Meanwhile, variable-resolution methods have been demonstrated to be beneficial in this context (co-kriging[60], two-level GPR[61]), also in combination with sequential sampling[62–65].

Recent performance-driven (or constrained) modeling[66] proposes a different manner of alleviating the problems of standard techniques by limiting the metamodel domain to a small district that contains increased-quality designs (w.r.t. the assumed figures of interest, e.g. operating frequencies). Domain confinement remarkably lowers computational expenditures of acquiring the training data without restricting the design utility of the model[67]. Constrained modeling comes in several variations that incorporate, among others, dimensionality reduction and variable-fidelity EM models[68–71]. The fundamental problem of the aforementioned techniques is an inflated initial cost associated with identification of the database designs, otherwise necessary to set up the domain of the surrogate[68]. To some extent, this issue can be mitigated by involving sensitivity information[72]. In[73], an alternate way to performance-driven modeling has been introduced, which abandons the use of reference designs in favor of random trial points. Information extracted therefrom is used to define the domain with the use of an auxiliary inverse regression model. The method of[73] has been shown to retain the benefits of constrained modeling which reduces the initial cost by almost seventy percent in some cases.

In this paper, we propose a novel antenna modeling approach, which employs the performance-driven paradigm, and advances over the reference-design-free approach presented in[73] by exploiting variable-resolution EM simulations. More specifically, generation of the trial points, necessary to identify the inverse regression model, is executed at the level of a coarse-discretization EM simulations. Furthermore, the majority of the training data points acquired to build the final metamodel are obtained at the same level, and supplemented by a small amount of high-fidelity samples. The data of both resolution levels is then blended using co-kriging[74]. Numerical validation performed using three antenna structures demonstrates that our framework allows to achieve additional computational savings of up to 64 percent over the technique of[73], and as high as 82 percent over the nested kriging framework[68] with regard to the model setup costs. This speedup is obtained without degrading the predictive power of the surrogate. Moreover, it ensures a remarkable accuracy improvement over conventional modeling methods.

Two-level variable-fidelity modeling within restricted domain. This section formulates the modeling methodology proposed in the paper. First, the concept of performance-driven modeling is recalled, along with an outline of the trial point acquisition (section "Performance-driven modeling basics"). In sections two-stage modeling: trial points and inverse regression model and surrogate domain definition, inverse regression model and surrogate domain definition are delineated, respectively. Section final surrogate. variable-resolution models and co-kriging discusses a construction of the final model using co-kriging, whereas section modeling procedure summary summarizes the complete procedure.

Performance-driven modeling basics. Here, we recall the basics of constrained (or performance-driven) modeling. The main concept is to construct the surrogate in a small portion of the parameter space, which encloses the designs being nearly optimum with regard to the target objective vectors. The computational benefits are due to a small volume of such a subset and a smaller sizes of training data sets that are needed to construct model of a satisfactory predictive power[75].

Table 1 outlines the notation used by constrained modeling frameworks[68]. The figures of interest may include antenna operating frequencies (but also the bandwidths or permittivity of a dielectric substrate). The central idea here pertains to the objective space F that determines the validity zone of the metamodel. Another important entity is the model domain. Its establishment involves the concept of design optimality, that is measured using a merit function $U(\boldsymbol{x}, \boldsymbol{f})$[69]. The solution $\boldsymbol{x}^*$, which is optimal with respect to a performance vector $\boldsymbol{f} \in F$, is given as

$$\mathbf{x}^* = U_F(\mathbf{f}) = \arg\min_{\mathbf{x}} U(\mathbf{x}, \mathbf{f}). \tag{1}$$

The optimum design manifold, consisting of designs (1) obtained for all $\boldsymbol{f} \in F$, constitutes an N-dimensional object in X, given as

$$U_F(F) = \{U_F(\mathbf{f}) : \mathbf{f} \in F\}. \tag{2}$$

The domain of the surrogate model is determined as a neighborhood of $U_F(F)$[69]. In a majority of performance-driven frameworks, its definition exploits database designs $\boldsymbol{x}^{(j)} = [x_1^{(j)} \ldots x_n^{(j)}]^T$, $j = 1, \ldots, p$, optimal with respect

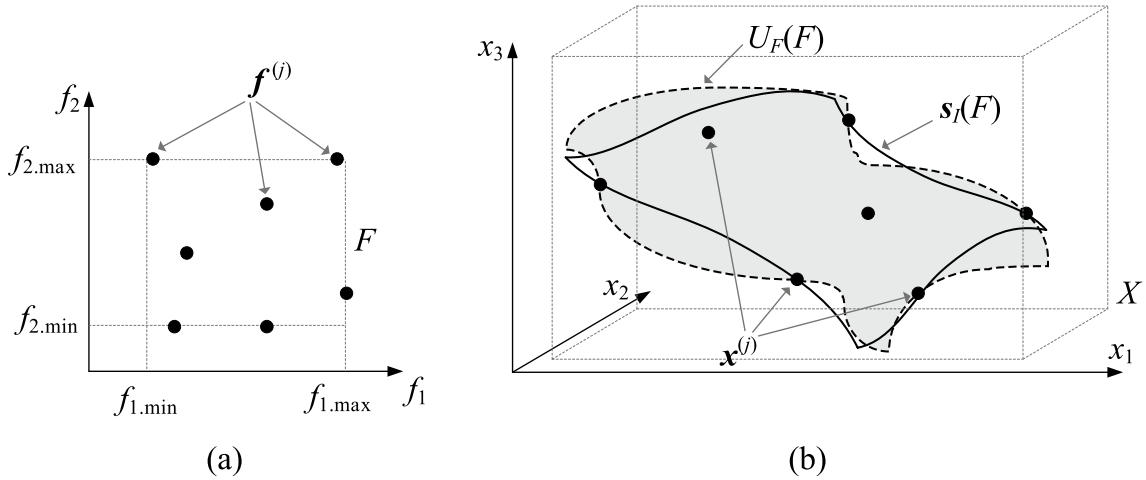

Figure 1. Basics of confined modeling[68]: (**a**) the objectives' space F, (**b**) design space X (black circles mark the trial points, grey surface indicates the manifold of optimum designs $U_F(F)$). The image of the first-layer metamodel $\boldsymbol{s}_l(F)$ yields a rough assessment of the manifold, so it needs to be outstretched to encompass entire $U_F(F)$.

to (1) for objective vectors $\boldsymbol{f}^{(j)} = [f_1^{(j)} \ldots f_N^{(j)}]$, distributed in F. More specifically, the couples $\{\boldsymbol{f}^{(j)}, \boldsymbol{x}^{(j)}\}$, $j = 1, \ldots, p$, serve as a training points to build the first-layer model $\boldsymbol{s}_l(\boldsymbol{f}) : F \rightarrow X$ [68] that approximates $U_F(F)$, see Fig. 1. The metamodel domain itself constitutes an orthogonal extension of the first-level surrogate[69].

Acquisition of the database designs is a bottleneck of performance-driven modeling procedures because it requires a large number (a few hundreds to over a thousand) of antenna simulations[73]. These extra expenses contribute to the overall model setup cost. As mentioned earlier, the number of trial points can be reduced by exploiting the sensitivity information[72], whereas their identification costs may be diminished by warm-start optimization algorithms (e.g.[76]).

The recent constrained modeling framework[73] introduced an alternative method for defining the model domain, which utilizes random trial points in place of the reference designs. The details of this method will be recalled in section two-stage modeling: trial points and inverse regression model, as it is one of the constituent parts of the introduced modeling procedure proposed.

Two-stage modeling: trial points and inverse regression model. First, we will define the surrogate model domain. Toward this end, we need to roughly assess the optimum design manifold $U_F(F)$ of Eq. (2). We follow the methodology of[73], where the required information is extracted from a set of random trial points, allocated in the design space X.

We denote by $\boldsymbol{x}_r^{(j)} = [x_{r.1}^{(k)} \ldots x_{r.n}^{(k)}]^T$, $j = 1, 2, \ldots$ a series of random trial points yielded according to a uniform probability distribution and by $\boldsymbol{f}_r^{(j)} = [f_{r.1}^{(j)} \ldots f_{r.N}^{(j)}]^T$ the performance figure vectors derived from the antenna response rendered by the full-wave model at $\boldsymbol{x}_r^{(j)}$. The performance figures are the same as the elements of the objective space F, e.g. the antenna resonant frequencies. The trial point is accepted if the extracted $\boldsymbol{f}_r^{(j)}$ resides in F and rejected otherwise (i.e. if the entries of $\boldsymbol{f}_r^{(j)}$ are located outside the lower and upper limits $f_{k.\min}$ and $f_{k.\max}$, cf. Table 1, or if $\boldsymbol{f}_r^{(j)}$ cannot be identified due to distorted antenna responses). Figure 2 gives a graphical illustration of the trial point selection for an exemplary dual-band antenna. The process of generating the trial points continues until the assumed number N_r (e.g. 50) has been identified. For each accepted point $\boldsymbol{x}_r^{(j)}$, an additional vector $\boldsymbol{p}_r^{(j)} = [p_{r.1}^{(j)} \ldots p_{r.M}^{(j)}]^T$ is extracted from antenna responses. The said vector $\boldsymbol{p}_r^{(j)}$ contains the information pertaining to antenna performance. In our example, these may refer to the reflection coefficient levels at the resonant frequencies, in which case $M = N$.

Using the set $\{\boldsymbol{x}_r^{(j)}, \boldsymbol{f}_r^{(j)}, \boldsymbol{p}_r^{(j)}\}_{j=1,\ldots,Nr}$, an inverse regression metamodel s_r: $F \rightarrow X$ is constructed, serving as a rough assessment of the manifold $U_F(F)$. The analytical form of the model is taken as (cf.[73])

$$s_r(\mathbf{f}) = \mathbf{s}_r\left([f_1 \ldots f_N]^{\mathrm{T}}\right) = \begin{bmatrix} s_{r.1}(\mathbf{f}) \\ \cdots \\ s_{r.n}(\mathbf{f}) \end{bmatrix} = \begin{bmatrix} a_{1.0} + a_{1.1} \exp\left(\sum_{k=1}^{N} a_{1.k+1} f_k\right) \\ \cdots \\ a_{n.0} + a_{n.1} \exp\left(\sum_{k=1}^{N} a_{n.k+1} f_k\right) \end{bmatrix}. \tag{3}$$

The rationale for adopting the specific analytical form of the inverse surrogate as in Eq. (3) is that it is sufficient to adequately reflect typically weakly-nonlinear relationships between the antenna geometry and operating parameters. Moreover, exponential terms feature only few parameters, and are flexible in the sense that they allow for modeling various curvatures, e.g. inverse proportionality occurring for certain parameters.

The coefficients of the inverse surrogate are found as the solutions of the following tasks.

MOST WIEDZY Downloaded from mostwiedzy.pl

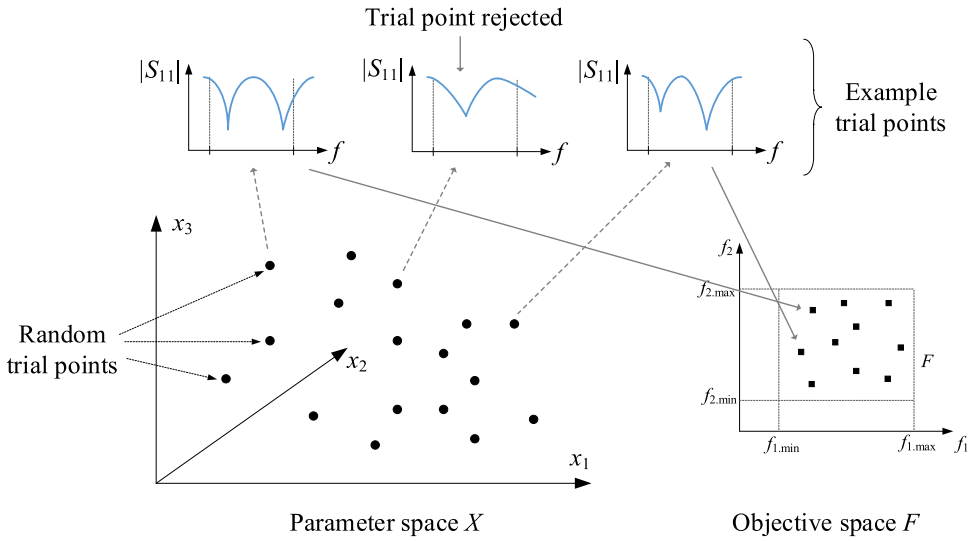

Figure 2. Procedure of the random trial point rendition for an exemplary dual-band antenna (the objective and parameter space are two- and three-dimensional, respectively). The random designs whose resonant frequencies reside within the required confines of the objective space are retained, the remaining ones are discarded. The inverse regression model $s_r(\cdot)$ is built using the ultimate trial point set $\{\boldsymbol{x}_r^{(j)}\}_{j=1,\ldots,N_r}$.

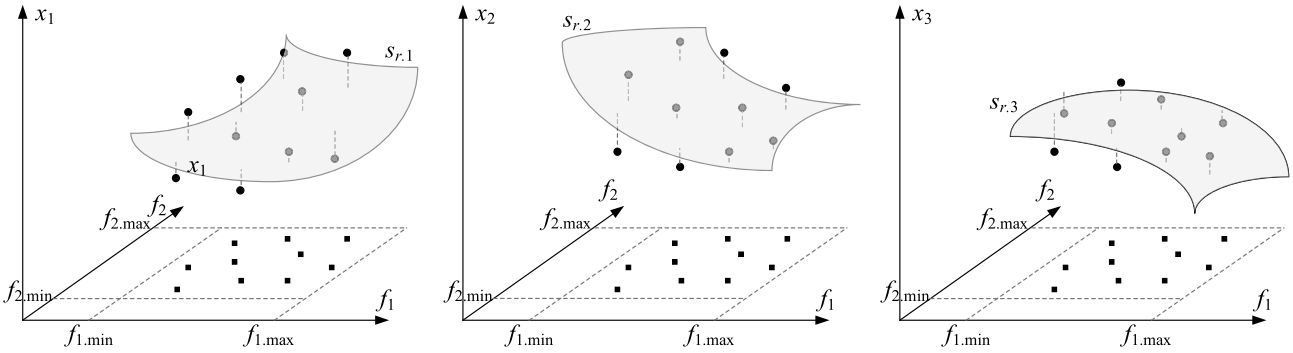

Figure 3. Inverse regression model s_r constructed based on the pre-selected trial points $\boldsymbol{x}_r^{(j)}$ along with their respective objectives $\boldsymbol{f}_r^{(j)}$. The model elements $s_{r.j}$ are are shown as grey surfaces for the parameters x_1 (left), x_2 (middle), and x_3 (right), respectively.

$$\left[a_{j.0}\ a_{j.1}\ \ldots\ a_{j.N+1}\right] = \arg \min_{[b_0\ b_1\ \ldots\ b_{K+1}]} \sum_{k=1}^{N_r} w_k \left[s_{r.j}\left(\mathbf{f}_r^{(k)}\right) - x_{r.j}^{(k)}\right]^2,\ \mathrm{j} = 1,\ldots,\mathrm{n}. \tag{4}$$

The weigh factors w_k are computed as

$$w_k = \left[W - \max\{p_1(\mathbf{x}^{(j)}),\ldots,p_N(\mathbf{x}^{(j)})\}\right]^2,\ \mathrm{k} = 1,\ldots,\mathrm{N}_r, \tag{5}$$

where $W = \max\{k = 1,\ldots,N_r, j = 1,\ldots,N: p_j^{(k)}\}$. Here, we assume that $p_j^{(k)} > 0$, and better designs are associated with lower values of $p_j^{(k)}$. The factors w_k are introduced to promote high-quality trial points so as to increase their contribution to the inverse model, which is because these vectors are located in a closer proximity of $U_F(F)$. Figure 3 shows graphically the concepts of the model s_r in accordance with the example of Fig. 2. Observe that the design space needs to be selected with a proper consideration with respect to the anticipated design quality therein, i.e. the ranges of the antenna geometry parameters have to be established reasonably. Otherwise, the number of trial points necessary to gather the assumed number of the observables of decent quality may be too excessive and thus, the computational benefits of the introduced technique may be compromised. In this work, we assume that the design space has been selected using at least a rudimentary problem-specific knowledge.

Surrogate domain definition. As discussed earlier, the set $s_r(F)$ approximates the manifold $U_F(F)$. The metamodel domain should contain a possibly large part of $U_F(F)$ so as to account for the designs being optimum (or close to optimum) with respect to all $\boldsymbol{f} \in F$. In[73], this is achieved by orthogonally extending $s_r(F)$ in all directions orthogonal to this set. Let us define a orthonormal basis of vectors normal to $s_r(F)$ at $\boldsymbol{f}$ as $\{\boldsymbol{v}_n^{(k)}(\boldsymbol{f})\}$,

$k=1,\ldots,n-N$. Let also $\boldsymbol{T}=[T_1 \ldots T_n]^T$ denote a vector of non-negative extension factors. Further, let us compute the coefficients of the extension

$$\boldsymbol{\alpha}(\mathbf{f}) = [\alpha_1(\mathbf{f}) \ldots \alpha_{n-N}(\mathbf{f})]^{\mathrm{T}} = \left[|\mathbf{Tv}_n^{(1)}(\mathbf{f})| \ \ldots \ |\mathbf{Tv}_n^{(n-N)}(\mathbf{f})|\right]^{\mathrm{T}}. \tag{6}$$

Using (6), the metamodel domain X_S is given as

$$X_S = \left\{ \begin{array}{c} \mathbf{x} = s_r(\mathbf{f}) + \sum_{k=1}^{n-N} \lambda_k \alpha_k(\mathbf{f}) \mathbf{v}_n^{(k)}(\mathbf{f}) : \mathbf{f} \in F, \\ -1 \le \lambda_k \le 1, \ k = 1, \ldots, n-N \end{array} \right\}. \tag{7}$$

The meaning of this definition is that X_S comprises of all designs given by (7), generated for every possible combination of the objective vectors from the space F and $\lambda_k \in [-1, 1]$, $k=1,\ldots,n-N$. Observe that the domain lateral bounds are the manifolds $S_+ = \left\{\mathbf{x} \in X : \mathbf{x} = s_r(\mathbf{f}) + \sum_{k=1}^{n-N} \alpha_k(\mathbf{f}) \mathbf{v}_n^{(k)}(\mathbf{f})\right\}$ and $S_- = \left\{\mathbf{x} \in X : \mathbf{x} = s_r(\mathbf{f}) - \sum_{k=1}^{n-N} \alpha_k(\mathbf{f}) \mathbf{v}_n^{(k)}(\mathbf{f})\right\}$.

The extension factors T_j are established individually for all parameters using the trial points $\{\boldsymbol{x}_r^{(j)}\}$ and the following procedure. We denote the kth parameter's lower and upper bounds as l_k and u_k, respectively. Given the pair $\{\boldsymbol{x}_r^{(j)}, \boldsymbol{f}_r^{(j)}\}$, we define $P_k(\boldsymbol{x}_r^{(j)}) \in [l_k \ u_k] \times F$ as the vector for which the distance between $[x_{r.k}^{(j)} \ (\boldsymbol{f}_r^{(j)})^T]^T$ and $[s_{r.k}(\boldsymbol{f}) \ \boldsymbol{f}^T]^T, \boldsymbol{f} \in F$, i.e.

$$P_k(\mathbf{x}_r^{(j)}) = \arg\min_{\mathbf{f} \in F} ||[x_{r.k}^{(j)} \ (\mathbf{f}_r^{(j)})^{\mathrm{T}}]^{\mathrm{T}} - [s_r(\mathbf{f}) \ \mathbf{f}^{\mathrm{T}}]^{\mathrm{T}}||, \tag{8}$$

is minimal; with the orthogonal projection of $[x_{r.k}^{(j)} \ (\boldsymbol{f}_r^{(j)})^T]^T$ onto the representation of $s_{r.k}$ in $[l_k \ u_k] \times F$ denoted as $P_k(\boldsymbol{x}_r^{(j)})$. Consequently

$$d_{r.k}(\mathbf{x}_r^{(j)}) = ||[x_{r.k}^{(j)} \ (\mathbf{f}_r^{(j)})^{\mathrm{T}}]^{\mathrm{T}} - [s_r(P(\mathbf{x}_r^{(j)})) \ P(\mathbf{x}_r^{(j)})^{\mathrm{T}}]^{\mathrm{T}}||, \tag{9}$$

refers to the minimal distance between the said image and $[x_{r.k}^{(j)} \ (\boldsymbol{f}_r^{(j)})^T]^T$ (note that $d_{r.k}$ may be viewed as the distance between the entries of the trial vector and the gray surfaces of Fig. 3). Based on these considerations, we define the extension factors T_k as

$$T_k = \frac{1}{2N_r} \sum_{j=1}^{N_r} d_{r.k}(\mathbf{x}_r^{(j)}). \tag{10}$$

Thus, T_k constitutes a half of the averaged distance from the trial point entry to the corresponding image of $s_{r.k}$. The value of the factor 0.5 is chosen because many trial points are of poor quality and using (full) average distance would lead to excessively large domain containing too many designs that are far from the optimum ones[73].

Final surrogate. variable-resolution models and co-kriging. One of the important mechanisms employed in this work to lower the cost of surrogate model construction are variable-resolution EM models. In most cases, the modeling process is executed at a single level of fidelity, except situations where the lower-resolution model is corrected with the use of a handful of high-fidelity samples (e.g. space mapping[77], co-kriging[74]). In this work, we employ low-fidelity models to accelerate the process of defining the surrogate model domain, as well as to downsize the training data acquisition cost.

Variable-resolution EM models. The fundamental benefit of using low-fidelity models, which typically means coarse-discretization EM simulations in the case of antennas[78], is that the associated simulation time may be considerably shortened, as compared to the high-fidelity version. The latter is normally established to ensure sufficiently accurate rendition of antenna characteristics. The speedup obtained due to low-fidelity analysis is obtained at the expense of the accuracy loss (cf. Fig. 4), which may or may not be problematic, depending on the particular context. For example, in space mapping optimization, the low-fidelity model should to be corrected to make it a reliable prediction tool, at least in the vicinity of the current iteration point[79]. When the low-fidelity model is used to, e.g. parameter space pre-screening, it can usually be used uncorrected[80].

In this work, the low-fidelity or coarse model, denoted as $\boldsymbol{R}_c(\boldsymbol{x})$, will be used for two purposes: (i) generation of the trial points and metamodel definition as delineated in section two-stage modeling: trial points and inverse regression model, and (ii) accelerating the acquisition of the training data by complementing sparsely-sampled high-fidelity model responses (denoted as $\boldsymbol{R}_f(\boldsymbol{x})$) with densely-sampled low-fidelity ones. In the case of (ii), co-kriging[74] is used to combine simulation data of different fidelities. As for (i), because the trial points are only employed to provide an inaccurate approximation of the manifold comprising optimum designs, there is no need to correct a low-fidelity model at this phase of the modeling process, which is advantageous from the standpoint of simplicity of implementation.

Final surrogate construction using co-kriging. The final surrogate $\boldsymbol{s}_{CO}(\boldsymbol{x})$ is generated in the domain X_S using co-kriging[60]. The training data set contains N_{Bf} high-fidelity pairs $\{\boldsymbol{x}_{Bf}^{(k)}, \boldsymbol{R}_f(\boldsymbol{x}_{Bf}^{(k)})\}_{k=1,\ldots,NBf}$, where $\boldsymbol{x}_{Bf}^{(k)} \in X_S$, and N_{Bc} low-fidelity pairs $\{\boldsymbol{x}_{Bc}^{(k)}, \boldsymbol{R}_c(\boldsymbol{x}_{Bc}^{(k)})\}_{k=1,\ldots,NBc}$, $\boldsymbol{x}_{Bc}^{(k)} \in X_S$. We also use notation $X_{Bf} = \{\boldsymbol{x}_{Bf}^{(k)}\}_{k=1,\ldots,NBf}$ and $X_{Bc} = \{\boldsymbol{x}_{Bc}^{(k)}\}_{k=1,\ldots,NBc}$.

MOST WIEDZY Downloaded from mostwiedzy.pl

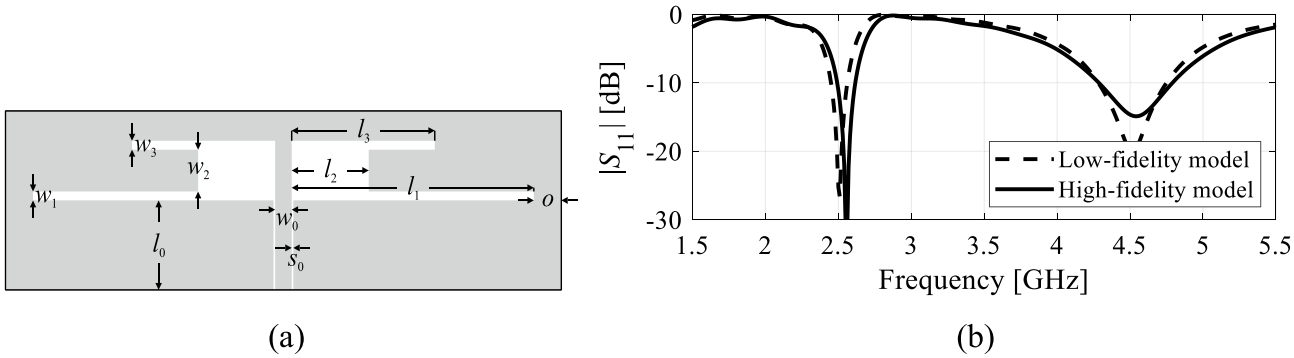

Figure 4. Variable-fidelity models: (**a**) an exemplary dual-band antenna, (**b**) antenna reflection responses evaluated with the low-fidelity EM model (- - -) and the high-fidelity one (—). Here, the high-fidelity model simulation time is about 80 s, whereas the time of the coarse model is only 25 s.

Let us begin by a recollection of the kriging interpolation, followed by formulation of co-kriging. The kriging surrogate $\boldsymbol{s}_{KR}(\boldsymbol{x})$ is given as

$$\mathbf{s}_{KR}(\mathbf{x}) = \mathbf{M}\gamma + r(\mathbf{x}) \cdot \boldsymbol{\Psi}^{-1} \cdot (\mathbf{R}_f(X_{Bf}) - \mathbf{F}\gamma), \tag{11}$$

with $\boldsymbol{M}$ being a $N_{Bf} \times t$ model matrix of X_{Bf}, whereas $\boldsymbol{F}$ denotes a row vector of the design $\boldsymbol{x}$ comprising t elements (t denotes the number of regression function factors[60]); and γ refer to coefficients of the regression function

$$\gamma = (X_{Bf}^T \boldsymbol{\Psi}^{-1} X_{Bf})^{-1} X_{Bf} \boldsymbol{\Psi}^{-1} \mathbf{R}_f(X_{Bf}). \tag{12}$$

We also have $r(\mathbf{x}) = (\psi(\mathbf{x}, \mathbf{x}_{Bf}^{(1)}), ..., \psi(\mathbf{x}, \mathbf{x}_{Bf}^{(N_{Bf})}))$, constitutes an N_{Bf}—element row vector whose entries are the correlations between X_{Bf} and $\boldsymbol{x}$, whereas $\boldsymbol{\Psi} = [\Psi_{i,j}]$ denotes a correlation matrix, where $\Psi_{i,j} = \psi(\boldsymbol{x}_{Bf}^{(i)}, \boldsymbol{x}_{Bf}^{(j)})$. An exemplary widely used correlation function may be

$$\psi(\mathbf{x}, \mathbf{x}') = \exp\left(\sum_{k=1}^{n} -\theta_k |x^k - x'^k|^P\right), \tag{13}$$

where θ_k, $k = 1, \ldots, n$, are the hyperparameters to be found during model identification, which is achieved through Maximum Likelihood Estimation (MLE)[60] as

$$(\theta_1, ..., \theta_n) = \arg\min -(N_{Bf}/2)\ln(\hat{\sigma}^2) - 0.5\ln(|\Psi|), \tag{14}$$

where $\hat{\sigma}^2 = (\mathbf{R}_f(X_{Bf}) - F\alpha)^T \boldsymbol{\Psi}^{-1} (\mathbf{R}_f(X_{Bf}) - F\alpha)/N_{Bf}$, with $|\boldsymbol{\Psi}|$ being the determinant of $\boldsymbol{\Psi}$. In practice, a correlation function of Gaussian type (P equal to 2) is often employed, as well as $\boldsymbol{M} = 1$ and $\boldsymbol{F} = [1 \ldots 1]^T$.

Co-kriging blends together two models: (i) a kriging surrogate $\boldsymbol{s}_{KRc}$ set up with the low-fidelity samples (X_{Bc}, $\boldsymbol{R}_c(X_{Bc})$) and (ii) the model $\boldsymbol{s}_{KRf}$ built using the residuals (X_{Bf}, $\boldsymbol{r}$), with $\boldsymbol{r} = \boldsymbol{R}_f(X_{Bf}) - \rho \cdot \boldsymbol{R}_c(X_{Bf})$. In the latter, ρ is a portion of the maximum likelihood estimate of the $\boldsymbol{s}_{KRf}$ surrogate. $\boldsymbol{R}_c(X_{Bf})$ is roughly equal to $\boldsymbol{s}_{KRc}(X_{Bf})$. The correlation function of the two models is described by Eq. (13).

The co-kriging model $\boldsymbol{s}_{CO}(\boldsymbol{x})$ is given by

$$\mathbf{s}_{CO}(\mathbf{x}) = \mathbf{M}\gamma + r(\mathbf{x}) \cdot \boldsymbol{\Psi}^{-1} \cdot (\mathbf{r} - \mathbf{F}\gamma), \tag{15}$$

where

$$r(\mathbf{x}) = [\rho \cdot \sigma_c^2 \cdot r_c(\mathbf{x}), \rho^2 \cdot \sigma_c^2 \cdot r_c(\mathbf{x}, X_{B_f}) + \sigma_d^2 \cdot r_d(\mathbf{x})] \tag{16}$$

$$\boldsymbol{\Psi} = \begin{bmatrix} \sigma_c^2 \boldsymbol{\Psi}_c(X_{Bc}, X_{Bc}) & \rho\, \sigma_c^2 \boldsymbol{\Psi}_c(X_{Bc}, X_{Bf}) \\ \rho\, \sigma_c^2 \boldsymbol{\Psi}_c(X_{Bf}, X_{Bc}) & \rho^2 \sigma_c^2 \boldsymbol{\Psi}_c(X_{Bf}, X_{Bf}) + \sigma_d^2 \boldsymbol{\Psi}_d \end{bmatrix}, \tag{17}$$

with $\boldsymbol{M} = [\rho \boldsymbol{M}_c\, \boldsymbol{M}_d]$, moreover matrices ($\boldsymbol{F}_c$, σ_c, $\boldsymbol{\Psi}_c$, $\boldsymbol{M}_c$) and ($\boldsymbol{F}_d$, σ_d, $\boldsymbol{\Psi}_d$, $\boldsymbol{M}_d$) are derived, in turn, from $\boldsymbol{s}_{KRc}$ and $\boldsymbol{s}_{KRf}$[60].

Design of experiments. A separate note should be made about the domain sampling procedure. Performing the design of experiments in a direct manner is inconvenient, as a geometry of the set X_S is relatively complex. Instead, we use the procedure explained in Fig. 5, which involves a surjective transformation between the unit cube $[0, 1]^n$ and the constrained domain. According to this procedure, the samples $\boldsymbol{x}_B^{(k)} = h_2(h_1(\boldsymbol{z}^{(k)})) \in X_S$ are uniformly distributed w.r.t. the objective space F, but not w.r.t. X_S. The normalized samples $\{\boldsymbol{z}^{(k)}\}$, $k = 1, \ldots, N_B$, are distributed using Latin Hypercube Sampling, LHS[81]). Observe that the proposed modeling technique belong to a wider class of performance-driven (or constrained) modeling techniques, in which the surrogate is constructed within a region of the design space confined from the point of view of the design objectives. In contrast to the conventional modeling techniques, in performance-driven modeling, the surrogate domain constitutes a thin set within the classical deign space delimited by the lower and upper bounds on the design variables. As

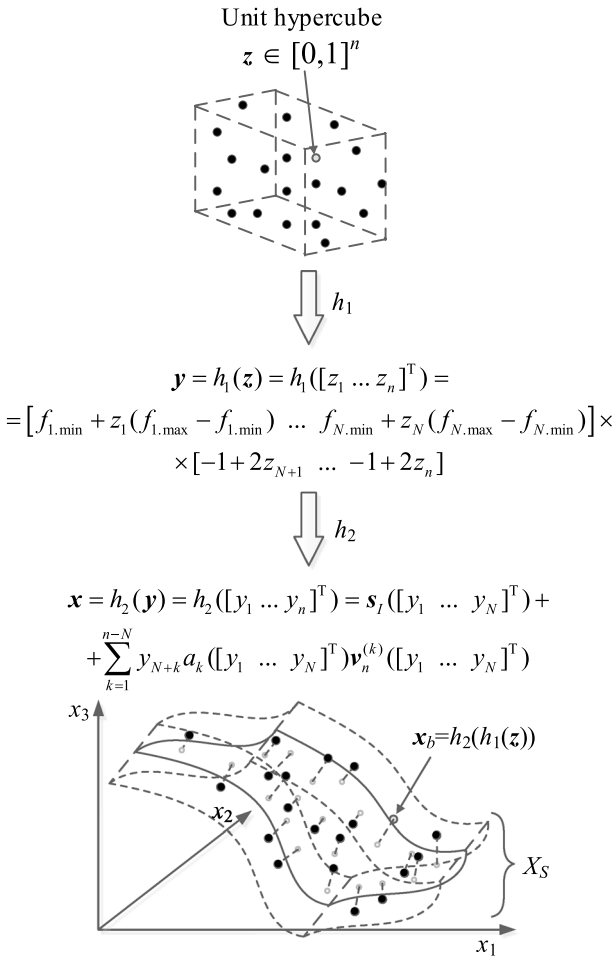

Figure 5. Conceptual illustration of the training data sampling process: (i) samples distributed according to Latin Hypercube Sampling (LHS)[81] (top), (ii) mapping onto the Cartesian product of the performance figure space F and $[-1,1]^{n-N}$ using function h_1 (middle), (iii) black circles mark data samples projected onto the confined domain X_S using function h_2 (bottom); gray circles indicate the samples distributed over the image of design space F prior to orthogonal extension.

demonstrated in[82], performing sequential sampling in a constrained domain does not bring any advantages over one-shot data sampling in terms of improving the model predictive power. This can be explained by a particular geometry of the constrained domain of the performance-driven surrogate, which encompasses nearly-optimum designs, the latter forming a manifold of a lower dimension than that of the original parameters space.

The function $h_2(h_1())$ also facilitates solving design tasks that involve the surrogate model, such as optimization. More specifically, the optimization process may be carried out over the unity cube $[0, 1]^n$, where the design variables (i.e. geometry parameters of the antenna at hand) are transformed into the model domain for metamodel evaluation. Additionally, $s_r(\boldsymbol{f})$ can be used as an initial design of a high quality for any assumed performance figure vector $\boldsymbol{f} \in F$.

It is expected that the incorporation of variable-fidelity models into the domain-confined surrogate, as described in this section, will lead to an additional computational savings over the method of[73] with regard to the total costs of the model setup. This is because majority of the costs (related to the acquisition of both the trial and training points) will be reduced by the factor equal to the EM simulation time ratio between the models of low- and high-fidelity.

Modeling procedure summary. Here, we summarize the proposed modeling procedure, the components of which were described in sections performance-driven modeling basics through final surrogate. variable-resolution models and co-kriging. It should be noted that there is only one control parameter, the number of trial points N_r, which is normally set to 50. The number of training data points (N_{Bf} of high-fidelity, and N_{Bc} of low-fidelity) depends on the required model accuracy. The modeling workflow has been provided in Fig. 6. Furthermore, Fig. 7 shows the flowchart of the process.

MOST WIEDZY Downloaded from mostwiedzy.pl

1. Acquire random trial points $\boldsymbol{x}_r^{(j)} \in X$. The process is continued until identifying N_r parameter vectors such that $\boldsymbol{f}_r^{(j)} \in F$ (cf. Section 2.2);
2. For all $\boldsymbol{x}_r^{(j)}$, evaluate performance vectors $\boldsymbol{p}_r^{(j)}$;
3. Identify the inverse regression model s_r using the dataset $\{\boldsymbol{x}_r^{(j)},\boldsymbol{f}_r^{(j)},\boldsymbol{p}_r^{(j)}\}_{j = 1,\ldots,Nr}$, (cf. (3)-(5));
4. Calculate the extension vector $\boldsymbol{T}$ as in (8)-(10), and the extension coefficients $\boldsymbol{\alpha}$ as in (6);
5. Define the surrogate model domain X_S using (7);
6. Perform design of experiments (see Fig. 4) to allocate N_{Bf} high-fidelity and N_{Bc} low-fidelity training points, $\boldsymbol{x}_{Bf}^{(k)}$ and $\boldsymbol{x}_{Bc}^{(k)}$, respectively;
7. Acquire low- and high-fidelity EM simulation data, $\boldsymbol{R}_c(\boldsymbol{x}_{Bc}^{(k)})\}_{k = 1, \ldots, NBc}$, and $\boldsymbol{R}_f(\boldsymbol{x}_{Bf}^{(k)})\}_{k = 1, \ldots, NBf}$;
8. Construct the final surrogate model $\boldsymbol{s}_{CO}$ using co-kriging. In the process, the trial-point set $\{\boldsymbol{x}_r^{(k)},\boldsymbol{R}_c(\boldsymbol{x}_r^{(k)})\}_{k = 1, \ldots, Nr}$ is included into the low-fidelity training data;

Figure 6. The workflow of the proposed antenna modeling procedure with variable-resolution EM simulations.

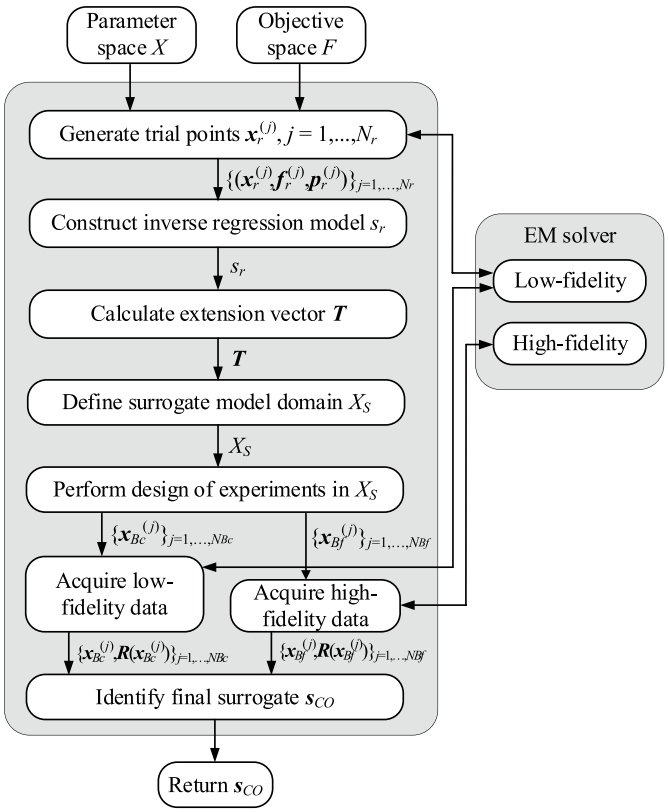

Figure 7. Operational flow of the presented two-layer modeling technique with domain confinement and variable-resolution EM simulations.

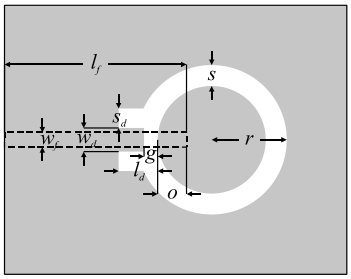

(a)

Parameter	Description
Substrate	ε_r – operating parameter, h = 0.76 mm
Design parameters$	$\boldsymbol{x} = [l_f\ l_d\ w_d\ r\ s\ s_d\ o\ g]^T$
Other parameters$	w_f – adjusted to ensure 50 ohm line impedance
Low-fidelity EM model	CST Microwave Studio (~120,000 cells, simulation time 30 s)
High-fidelity EM model	CST Microwave Studio (~300,000 cells, simulation time 90 s)
Figures of interest	Operating frequency f_0, substrate permittivity ε_r
Objective space	2.5 GHz ≤ f_0 ≤ 6.5 GHz, 2.0 ≤ ε_r ≤ 5.0
Design optimality	Minimum reflection at the target operating frequency and substrate permittivity
Conventional parameter space X	$\boldsymbol{l}$ = [22.0 3.5 0.3 6.5 3.0 0.5 3.5 0.2]^T, $\boldsymbol{u}$ = [27.0 8.0 2.3 16.0 7.0 5.5 6.0 2.3]^T
Modelled characteristics	Reflection response S_{11}

$ Dimensions in mm.

(b)

Figure 8. Antenna I: ring-slot microstrip antenna: (**a**) antenna geometry, (**b**) antenna parameters.

Results

The modeling procedure introduced in section two-level variable-fidelity modeling within restricted domain has been validated in this section with the use of three exemplary microstrip antennas. The results obtained for various training data set sizes are compared to a number of benchmark methods including traditional (i.e. unconstrained) metamodels (kriging and RBF), along with the performance-driven frameworks (nested kriging[68], and the reference-design-free approach[73]). The major figures of interest include the surrogates' predictive power, its dependence on the cardinality of the training dataset, as well as the computational cost of the model setup.

Verification antennas. The antenna structures used for verification have been shown in Figs. 8, 9 and 10. These include a ring-slot antenna[83], a dual-band dipole[84], and a quasi-Yagi antenna with a parabolic reflector[85], which henceforth are referred to as Antenna I, II and III, respectively. Figures 8, 9 and 10 also contain the relevant data, among others, designable parameters, operating parameters, and the details on the parameter and objective spaces. Furthermore, Fig. 11 shows the families of reflection responses corresponding to various model fidelities for all the benchmark antenna structures. Observe that all the benchmark antennas have been already validated, first, in their respective source papers[83–85], and also in our previous work, e.g.[68,86]). Therefore, the experimental validation has not been provided, as being immaterial to the scope of the paper.

Validation experiments setup. Antennas I, II and III have been modelled utilizing the technique proposed in this paper, as well as a number of benchmark methods, as listed in Table 2. The benchmark surrogates have been built using the training sets comprising 50, 100, 200, 400 and 800 data samples. The proposed models were obtained using several combinations of the coarse and fine datasets, in particular, N_{Bf} = 50 and $N_{Bc} \in \{50, 100, 200, 400, 800\}$, as well as N_{Bf} = 100 and $N_{Bc} \in \{50, 100, 200, 400, 800\}$. The cost of model construction is calculated in terms of the equivalent number of high-fidelity simulations, which considers the simulation time ratio of $\boldsymbol{R}_f$ versus $\boldsymbol{R}_c$. Also, the cost includes all additional expenses, e.g. those associated with the reference database designs acquisition for the nested kriging framework[68], or generating the trial points for the method of[73], and the introduced technique.

A relative RMS error has been used as a measure of the model accuracy. It has been computed as $||\boldsymbol{R}_s(\boldsymbol{x})-\boldsymbol{R}_f(\boldsymbol{x})||/||\boldsymbol{R}_f(\boldsymbol{x})||$, where $\boldsymbol{R}_s$ and $\boldsymbol{R}_f$ are the surrogate and EM-simulated antenna characteristics, respectively. The average errors are reported, which are obtained for one hundred independent testing points.

Discussion

The results can be found in Tables 3, 4 and 5, for Antenna I, II and III, respectively. Furthermore, Figs. 12, 13 and 14 illustrate the antenna responses at selected test locations, evaluated using the proposed model and EM simulation. The analysis of the data in the tables leads to the following observations:

MOST WIEDZY Downloaded from mostwiedzy.pl

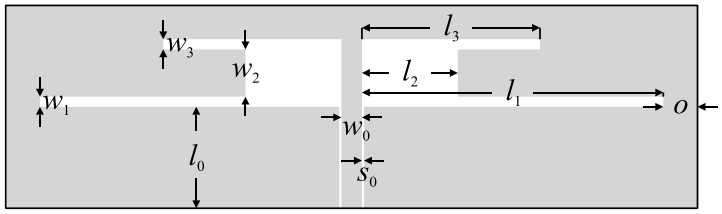

(a)

Parameter	Description
Substrate	RO4350 (ε_r = 3.5, h = 0.76 mm)
Design parameters$	$\boldsymbol{x} = [l_1\ l_2\ l_3\ w_1\ w_2\ w_3]^T$
Other parameters$	$l_0 = 30$, $w_0 = 3$, $s_0 = 0.15$, $o = 5$
Low-fidelity EM model	CST Microwave Studio (~40,000 cells, simulation time 25 s)
High-fidelity EM model	CST Microwave Studio (~150,000 cells, simulation time 80 s)
Figures of interest	Operating frequencies f_1 and f_2
Objective space	2.0 GHz ≤ f_1 ≤ 3.0 GHz, 4.0 GHz ≤ f_2 ≤ 5.5 GHz
Design optimality	Minimum reflection at both operating frequencies
Conventional parameter space X	$\boldsymbol{l} = [29\ 5.0\ 17\ 0.2\ 1.5\ 0.5]^T$, $\boldsymbol{u} = [42\ 12\ 25\ 0.6\ 5.2\ 3.5]^T$
Modelled characteristics	Reflection response S_{11}

$ Dimensions in mm.

(b)

Figure 9. Antenna II: dual-band uniplanar dipole antenna: (**a**) antenna geometry, (**b**) antenna parameters.

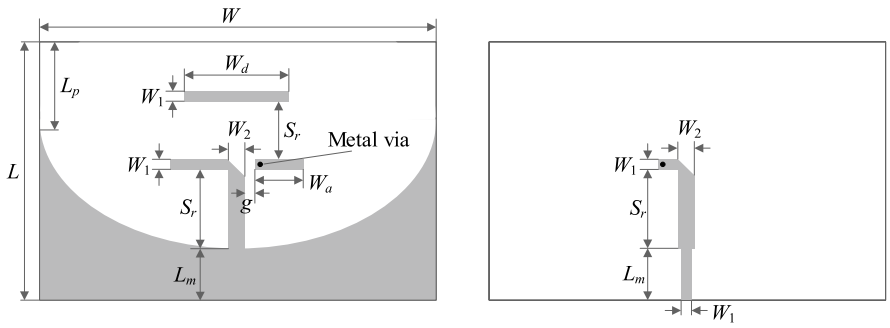

(a)

Parameter	Description
Substrate	ε_r – operating parameter, h = 1.5 mm
Design parameters$	$\boldsymbol{x} = [W\ L\ L_m\ L_p\ S_d\ S_r\ W_2\ W_a\ W_d\ g]$
Other parameters$	W_1 – adjusted to ensure 50 ohm line impedance
Low-fidelity EM model	CST Microwave Studio (~150,000 cells, simulation time 80 s)
High-fidelity EM model	CST Microwave Studio (~850,000 cells, simulation time 300 s)
Figures of interest	Operating frequency f_0, substrate permittivity ε_r
Objective space	2.5 GHz ≤ f_0 ≤ 5.0 GHz, 2.5 ≤ ε_r ≤ 4.5
Design optimality	Maximum realized gain in 8% fractional bandwidth centred at f_0; Constraint: $\lvert S_{11}\rvert \le -10$ dB at the same bandwidth
Conventional parameter space X	$\boldsymbol{l} = [100\ 55\ 10\ 14.5\ 6.0\ 10\ 2.0\ 7.5\ 16.3\ 0.5]^T$, $\boldsymbol{u} = [137\ 81\ 29\ 28\ 21\ 18\ 5.0\ 20\ 40\ 1.0]^T$
Modelled characteristics	Reflection response S_{11}, Realized gain G

$ Dimensions in mm.

(b)

Figure 10. Antenna III: qasi-Yagi antenna with parabolic reflector: (**a**) antenna geometry, (**b**) antenna parameters.

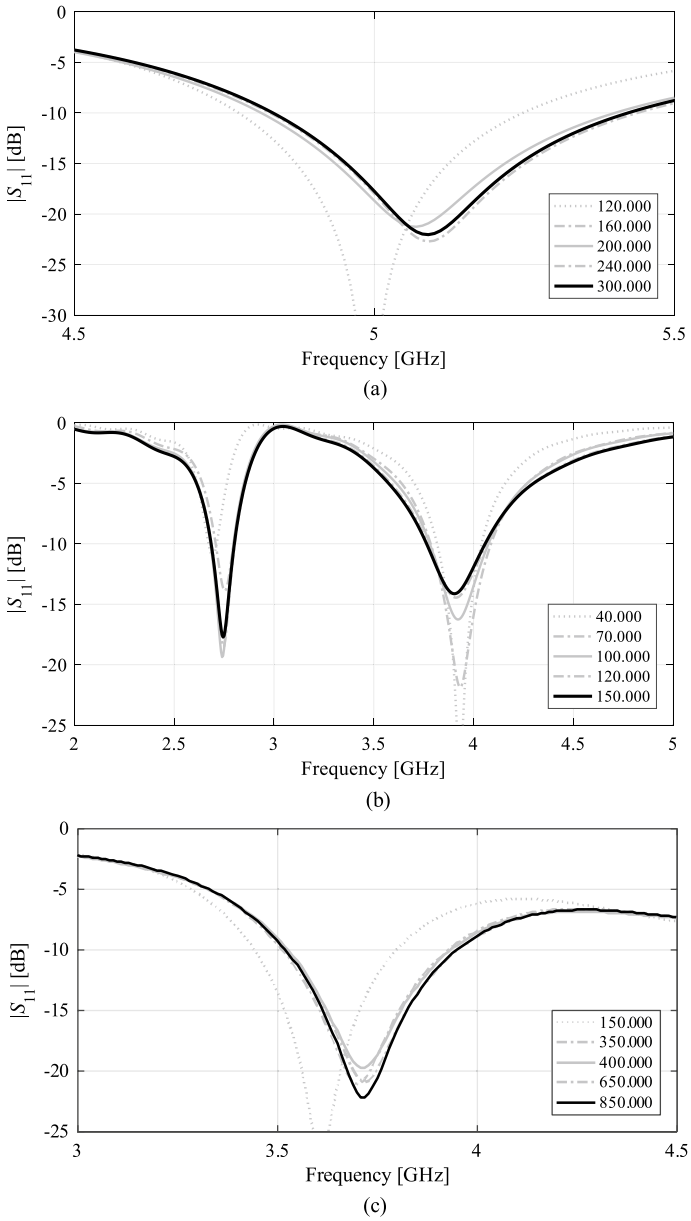

Figure 11. Grid convergence plots for: (**a**) Antenna I, (**b**) Antenna II, and (**c**) Antenna III for different numbers of mesh cells corresponding to various model fidelities from the lowest employed fidelity up to the highest one.

Modeling approach	Domain	Setup
Kriging interpolation	Conventional (parameter space X)	Gaussian correlation function, second-order polynomial used as a trend function
Radial basis functions (RBF)	Conventional (parameter space X)	Gaussian correlation function, scaling coefficient determined through cross-validation
Nested kriging[81]	Confined domain X_S	Thickness parameter $T = 0.05$ (Antennas I through III), 10 reference designs used in all cases, the numbers of EM simulations required for their identification: • Antenna I (acquisition cost 864 EM simulations) • Antenna II (acquisition cost 930 EM simulations) • Antenna III (acquisition cost 1899 EM simulations)
Reference-design-free modelling[65]	Confined domain X_S	Thickness parameter $T = 0.05$ (Antennas I through III), the following numbers of EM simulation used to identify $N_r = 50$ accepted observables: • 106 (Antenna I) • 230 (Antenna II) • 192 (Antenna III)

Table 2. Benchmark modeling methods.

MOST WIEDZY Downloaded from mostwiedzy.pl

Modeling method	Number of training samples[e]				
	50	100	200	400	800
Kriging					
Modeling error	56.9%	50.8%	35.8%	31.5%	25.6%
Model setup cost[b]	50	100	200	400	800
Modeling error	61.0%	53.2%	37.9%	34.1%	27.2%
RBF					
Model setup cost[b]	50	100	200	400	800
Modeling error	19.4%	12.9%	7.7%	5.1%	3.7%
Nested kriging[68]					
Model setup cost[a]	914	964	1064	1264	1664
Modeling error	13.4%	9.9%	6.9%	5.4%	4.4%
No-reference-design modeling[73]					
Model setup cost[c]	156	206	306	506	906
Modeling error	13.1%	8.5%	6.7%	5.1%	4.3%
Two-stage variable-resolution surrogate (this work)					
N_{Bf} **= 50**					
Model setup cost[d]	106.7	123.3	156.7	223.3	356.7
Modeling error	8.2%	7.7%	5.3%	4.2%	3.5%
N_{Bf} **= 100**					
Model setup cost[d]	156.7	173.3	206.7	273.3	406.7

Table 3. Antenna I: modeling results and benchmarking. [a]The cost includes acquisition of the reference designs, which is 864 EM high-fidelity simulations of the antenna when using feature-based optimization[67] as listed in the table. Conventional (minimax) optimization required high-fidelity 1012 simulations. [b]The cost refers to high-fidelity simulations. [c]The cost includes generation of random trial points, here, 106 high-fidelity simulations in total to yield $N_r = 50$ accepted samples. [d]The cost includes generation of random trial points at low-fidelity level, here, 120 simulations in total to yield $N_r = 50$ accepted samples. [e]In the case of the proposed model, the numbers 50 through 800 refer to low-fidelity EM simulations.

- The accuracy of the presented model outperforms that of the conventional (i.e. unconstrained) models. In particular, for Antennas I and III, the unconstrained surrogates are unable to yield the surrogates of usable accuracy: the modeling error is still beyond 25% even for the training sets of the largest sizes.
- The predictive power of the introduced surrogate is also better than for the nested kriging metamodel[68] set up using smaller training data sets, which is due to the inclusion of the random trial points into the training dataset. For larger values of N_B, the models exhibit similar accuracy. This is also the case for the reference-design-free method, the accuracy of which is comparable to the proposed model due to sharing the rules for model domain definition. Yet, for the smaller training sets, the proposed model is more accurate, which is because the overall number of samples (low- and high-fidelity together) is larger than for the method of[73]. Perhaps the most important advantage of the proposed methodology is an excellent computational efficiency. Executing majority of the operations with the use of low-fidelity model leads to considerable savings, as reported in Tables 3, 4 and 5. For example, the cost reduction over conventional surrogates is as high as 55, 54 and 60 percent for Antennas I, II and III, respectively, assuming $N_B = 800$ and $N_{Bf} = 50$.
- The savings over the nested kriging model are even higher due to the extra expenses entailed by the reference design acquisition in[68]. We have 78, 79 and 88 percent savings for Antennas I through III, respectively, also for $N_B = 800$ and $N_{Bf} = 50$. The savings over the reference-design-free methods[73] are 61, 64 and 68 percent, for Antenna I, II and III, respectively, again assuming $N_B = 800$ and $N_{Bf} = 50$. It should be reiterated that the cost reduction with respect to the benchmark performance-driven methods does not deteriorate the modeling accuracy.

Conclusion

This work presented a novel framework for surrogate modeling of antenna structures. Our approach exploits a constrained modeling paradigm with the surrogate model domain established using random trial points and the operating parameter data extracted therefrom. Furthermore, variable-resolution EM models are used at the domain definition stage and the surrogate construction phase. The latter combines sparsely acquired data samples of high-fidelity with densely collected low-fidelity training points. The final surrogate is rendered using co-kriging. Extensive numerical experiments confirm that the proposed method outperforms conventional methods. Furthermore, the predictive power of the presented surrogate is comparable or slightly better than for the benchmark performance-driven models. In terms of the computational efficiency, our modeling framework by far outperforms all the techniques employed in the numerical studies, both the conventional and the

Modeling method	Number of training samples[e]				
	50	100	200	400	800
Kriging					
Modeling error	21.7%	17.3%	12.6%	9.3%	7.2%
Model setup cost[b]	50	100	200	400	800
Modeling error	24.9%	19.8%	14.3%	10.5%	8.7%
RBF					
Model setup cost[b]	50	100	200	400	800
Modeling error	9.9%	6.4%	4.4%	3.8%	3.4%
Nested kriging[68]					
Model setup cost[a]	980	1030	1130	1330	1730
Modeling error	7.3%	5.1%	3.8%	3.1%	2.5%
No-reference-design modeling[73]					
Model setup cost[c]	280	330	430	630	1,030
Modeling error	5.4%	3.1%	2.5%	2.1%	1.7%
Two-stage variable-resolution surrogate (this work)					
N_{Bf} = 50					
Model setup cost[d]	132.8	148.4	179.7	242.2	367.2
Modeling error	3.5%	3.0%	2.3%	1.8%	1.6%
N_{Bf} = 100					
Model setup cost[d]	182.8	198.4	229.7	292.2	417.2

Table 4. Antenna II: modeling results and benchmarking. [a]The cost includes acquisition of the reference designs, which is 930 EM high-fidelity simulations of the antenna when using feature-based optimization[67] as listed in the table. Conventional (minimax) optimization required 1201 high-fidelity simulations. [b]The cost refers to high-fidelity simulations. [c]The cost includes generation of random observables, here, 230 high-fidelity simulations in total to yield $N_r = 50$ accepted samples. [d]The cost includes generation of random trial points at low-fidelity level, here, 215 simulations in total to yield $N_r = 50$ accepted samples. [e]In the case of the proposed model, the numbers 50 through 800 refer to low-fidelity EM simulations.

Modeling method	Number of training samples[e]				
	50	100	200	400	800
Kriging					
Modeling error	61.4%	50.7%	39.8%	32.8%	31.8%
Model setup cost[b]	50	100	200	400	800
RBF					
Modeling error	65.3%	51.8%	43.2%	37.1%	33.6%
Model setup cost[b]	50	100	200	400	800
Nested kriging[68]					
Modeling error	17.9%	13.3%	7.5%	5.4%	4.5%
Model setup cost[a]	1949	1999	2099	2299	2699
No-reference-design modeling[73]					
Modeling error	10.8%	8.4%	7.1%	5.9%	5.0%
Model setup cost[c]	242	292	392	592	992
Two-stage variable-resolution surrogate (this work)					
N_{Bf} = 50					
Modeling error	8.7%	7.2%	6.7%	6.5%	6.0%
Model setup cost[d]	118.5	131.9	158.5	211.9	318.5
N_{Bf} = 100					
Modeling error	6.8%	6.1%	5.4%	5.3%	5.2%
Model setup cost[d]	168.5	181.9	208.5	261.9	368.5

Table 5. Antenna III: modeling results and benchmarking. [a]The cost includes acquisition of the reference designs, which is 1899 EM high-fidelity simulations of the antenna. [b]The cost refers to high-fidelity simulations. [c]The cost includes generation of random trial points, here, 192 high-fidelity simulations in total to yield $N_r = 50$ accepted samples. [d]The cost includes generation of random trial points at low-fidelity level, here, 207 simulations in total to yield $N_r = 50$ accepted samples. [e]In the case of the proposed model, the numbers 50 through 800 refer to low-fidelity EM simulations.

MOST WIEDZY Downloaded from mostwiedzy.pl

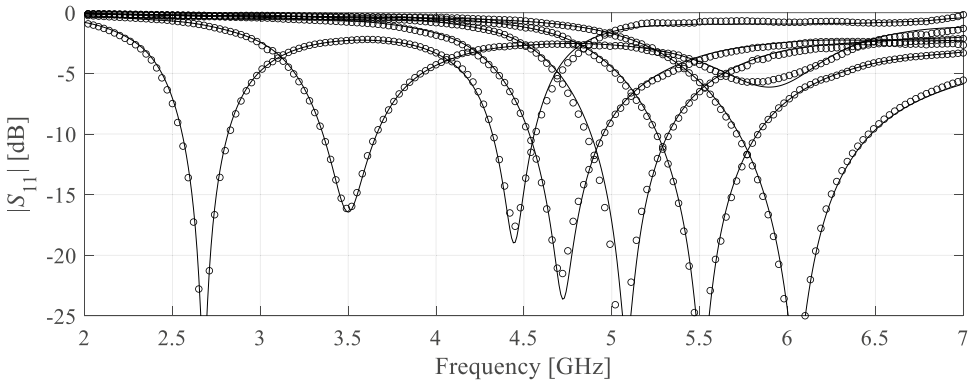

Figure 12. Antenna I: reflection responses at the representative test designs: full-wave model (—), and the presented two-level variable-fidelity surrogate (o) with N_{Bf} = 50 and N_{Bc} = 800.

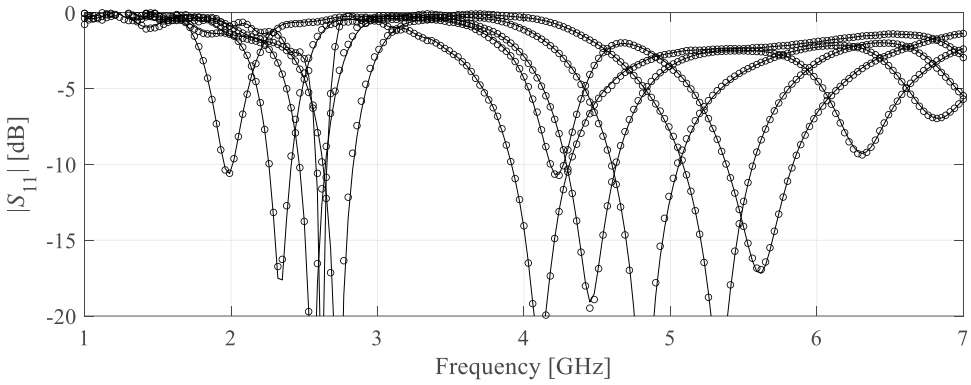

Figure 13. Antenna II: reflection responses at the representative test designs: full-wave model (—), and the presented two-level variable-fidelity surrogate (o) with N_{Bf} = 50 and N_{Bc} = 800.

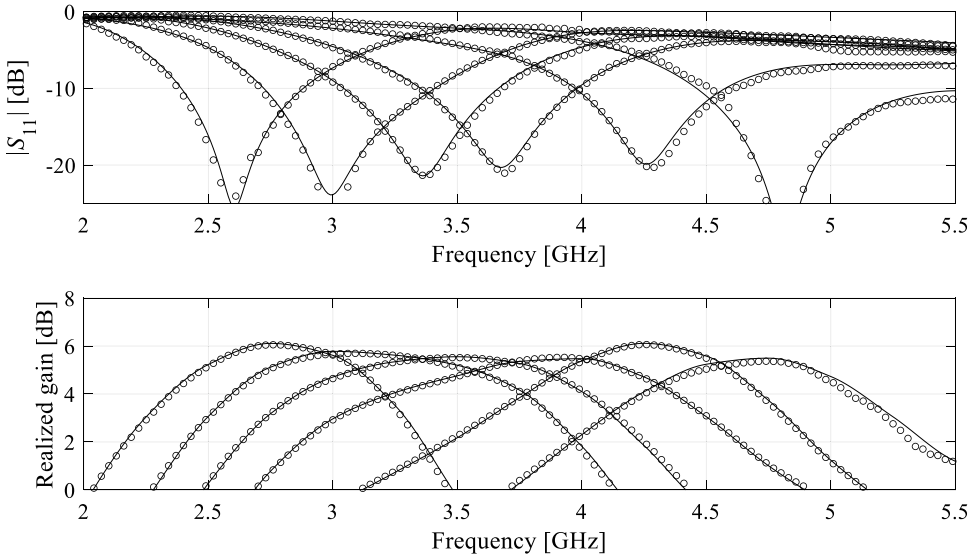

Figure 14. Antenna III: reflection responses at the representative test designs: full-wave model (—), and the presented two-level variable-fidelity surrogate (o) with N_{Bf} = 50 and N_{Bc} = 800.

performance-driven ones. The computational savings over the traditional models are as high as 56 percent on the average, whereas they are 82 and 64 percent over the nested kriging modeling technique and the database-design-free method, respectively. The procedure presented in this work can be considered a viable alternative to state-of-the-art modeling routines, especially for more demanding conditions that include multi-dimensional spaces with broad geometry and material parameters' ranges, the same pertains to the operating conditions.

Data availability

The datasets generated during and/or analysed during the current study are available from the corresponding author on reasonable request.

Received: 4 July 2022; Accepted: 14 September 2022
Published online: 14 October 2022

References

1. Lu, K. & Leung, K. W. On the circularly polarized parallel-plate antenna. *IEEE Trans. Antennas Propag.* **68**(1), 3–12 (2020).
2. Famoriji, O. J. & Xu, Z. Antenna feed array synthesis for efficient communication systems. *IEEE Sensors J.* **20**(24), 15085–15098 (2020).
3. Jonsson, B. L. G., Shi, S., Wang, L., Ferrero, F. & Lizzi, L. On methods to determine bounds on the Q-factor for a given directivity. *IEEE Trans. Antennas Propag.* **65**(11), 5686–5696 (2017).
4. Ullah, U. & Koziel, S. A broadband circularly polarized wide-slot antenna with a miniaturized footprint. *IEEE Antennas Wirel. Propag. Lett.* **17**(12), 2454–2458 (2018).
5. Nie, L. Y., Lin, X. Q., Yang, Z. Q., Zhang, J. & Wang, B. Structure-shared planar UWB MIMO antenna with high isolation for mobile platform. *IEEE Trans. Antennas Propag.* **67**(4), 2735–2738 (2019).
6. Wen, D., Hao, Y., Munoz, M. O., Wang, H. & Zhou, H. A compact and low-profile MIMO antenna using a miniature circular high-impedance surface for wearable applications. *IEEE Trans. Antennas Propag.* **66**(1), 96–104 (2018).
7. Krishna, A., Abdelaziz, A. F. & Khattab, T. Patch antenna array designs for wireless communication applications inside jet engines. *IEEE Trans. Antennas Propag.* **67**(2), 971–979 (2019).
8. Lei, S. *et al.* Power gain optimization method for wide-beam array antenna via convex optimization. *IEEE Trans. Antennas Propag.* **67**(3), 1620–1629 (2019).
9. Cui, J., Zhang, A. & Chen, X. An omnidirectional multiband antenna for railway application. *IEEE Antennas Wirel. Propag. Lett.* **19**(1), 54–58 (2020).
10. Wang, J., Wong, H., Ji, Z. & Wu, Y. Broadband CPW-fed aperture coupled metasurface antenna. *IEEE Antennas Wirel. Propag. Lett.* **18**(3), 517–520 (2019).
11. Das, G., Sharma, A., Gangwar, R. K. & Sharawi, M. S. Performance improvement of multiband MIMO dielectric resonator antenna system with a partially reflecting surface. *IEEE Antennas Wirel. Propag. Lett.* **18**(10), 2105–2109 (2019).
12. Feng, Y. *et al.* Cavity-backed broadband circularly polarized cross-dipole antenna. *IEEE Antennas Wirel. Propag. Lett.* **18**(12), 2681–2685 (2019).
13. Liu, J. *et al.* A wideband pattern diversity antenna with a low profile based on metasurface. *IEEE Antennas Wirel. Propag. Lett.* **20**(3), 303–307 (2021).
14. Liu, N. *et al.* Cross-polarization reduction of a shorted patch antenna with broadside radiation using a pair of open-ended stubs. *IEEE Trans. Antennas Propag.* **68**(1), 13–20 (2020).
15. Le, T. T., Tran, H. H. & Park, H. C. Simple-structured dual-slot broadband circularly polarized antenna. *IEEE Antennas Wirel. Propag. Lett.* **17**(3), 476–479 (2018).
16. Duan, J. & Zhu, L. An EH0-mode microstrip leaky-wave antenna with transversal single beam via periodical loading of shorting pins and U-shaped slots. *IEEE Antennas Wirel. Propag. Lett.* **19**(12), 2187–2191 (2020).
17. Wei, K., Li, J. Y., Wang, L., Xu, R. & Xing, Z. J. A new technique to design circularly polarized microstrip antenna by fractal defected ground structure. *IEEE Trans. Antennas Propag.* **65**(7), 3721–3725 (2017).
18. Kovaleva, M., Bulger, D. & Esselle, K. P. Comparative study of optimization algorithms on the design of broadband antennas. *IEEE J. Multiscale Multiphysics Comp. Techn.* **5**, 89–98 (2020).
19. Easum, J. A., Nagar, J., Werner, P. L. & Werner, D. H. Efficient multiobjective antenna optimization with tolerance analysis through the use of surrogate models. *IEEE Trans. Antennas Propag.* **66**(12), 6706–6715 (2018).
20. Du, J. & Roblin, C. Stochastic surrogate models of deformable antennas based on vector spherical harmonics and polynomial chaos expansions: Application to textile antennas. *IEEE Trans. Antennas Propag.* **66**(7), 3610–3622 (2018).
21. Pietrenko-Dabrowska, A., Koziel, S. & Al-Hasan, M. Expedited yield optimization of narrow- and multi-band antennas using performance-driven surrogates. *IEEE Access* **8**, 143104–143113 (2020).
22. Kouassi, A. *et al.* Reliability-aware optimization of a wideband antenna. *IEEE Trans. Antennas Propag.* **64**(2), 450–460 (2016).
23. Liu, Y., Li, M., Haupt, R. L. & Guo, Y. J. Synthesizing shaped power patterns for linear and planar antenna arrays including mutual coupling by refined joint rotation/phase optimization. *IEEE Trans. Antennas Propag.* **68**(6), 4648–4657 (2020).
24. Li, Q., Chu, Q., Chang, Y. & Dong, J. Tri-objective compact log-periodic dipole array antenna design using MOEA/D-GPSO. *IEEE Trans. Antennas Propag.* **68**(4), 2714–2723 (2020).
25. Zhu, D. Z., Werner, P. L. & Werner, D. H. Design and optimization of 3-D frequency-selective surfaces based on a multiobjective lazy ant colony optimization algorithm. *IEEE Trans. Antennas Propag.* **65**(12), 7137–7149 (2017).
26. Hosseininejad, S. E., Komjani, N. & Mohammadi, A. Accurate design of planar slotted SIW array antennas. *IEEE Antennas Wirel. Propag. Lett.* **14**, 261–264 (2015).
27. Nadia, C., Tomader, M. & Benbrahim, M. Array antenna characteristics improvement: Parasitic patches (two disposals) and multilayer substrate techniques. in *International Conference on Optimization and Applications (ICOA)* 1–6 (Mohammedia, Morocco, 2018).
28. Kalantari, L. S. & Bakr, M. H. Wideband cloaking of objects with arbitrary shapes exploiting adjoint sensitivities. *IEEE Trans. Antennas Propag.* **64**(5), 1963–1968 (2016).
29. Feng, F. *et al.* Coarse- and fine-mesh space mapping for EM optimization incorporating mesh deformation. *IEEE Microw. Wirel. Comp. Lett.* **29**(8), 510–512 (2019).
30. Koziel, S. & Pietrenko-Dabrowska, A. Reduced-cost electromagnetic-driven optimization of antenna structures by means of trust-region gradient-search with sparse Jacobian updates. *IET Microw. Antennas Propag.* **13**(10), 1646–1652 (2019).
31. Koziel, S. & Pietrenko-Dabrowska, A. Variable-fidelity simulation models and sparse gradient updates for cost-efficient optimization of compact antenna input characteristics. *Sensors* **19**(8), 1806 (2019).
32. Wang, J., Yang, X. S. & Wang, B. Z. Efficient gradient-based optimization of pixel antenna with large-scale connections. *IET Microw. Antennas Prop.* **12**(3), 385–389 (2018).

MOST WIEDZY Downloaded from mostwiedzy.pl

33. Xu, J., Li, M. & Chen, R. Space mapping optimisation of 2D array elements arrangement to reduce the radar cross-scattering. *IET Microw. Antennas Propag.* **11**(11), 1578–1582 (2017).
34. Su, Y., Li, J., Fan, Z. & Chen, R. *Shaping Optimization of Double Reflector Antenna Based on Manifold Mapping* 1–2 (International Applied Computational Electromagnetics Society Symposium (ACES), 2017).
35. Koziel, S., Ogurtsov, S., Cheng, Q. S. & Bandler, J. W. Rapid EM-based microwave design optimization exploiting shape-preserving response prediction and adjoint sensitivities. *IET Microw. Antennas Propag.* **8**(10), 775–781 (2014).
36. Koziel, S. & Unnsteinsson, S. D. Expedited design closure of antennas by means of trust-region-based adaptive response scaling. *IEEE Antennas Wirel. Propag. Lett.* **17**(6), 1099–1103 (2018).
37. Salucci, M., Tenuti, L., Oliveri, G. & Massa, A. Efficient prediction of the EM response of reflectarray antenna elements by an advanced statistical learning method. *IEEE Trans. Antennas Propag.* **66**(8), 3995–4007 (2018).
38. Dong, J., Qin, W. & Wang, M. Fast multi-objective optimization of multi-parameter antenna structures based on improved BPNN surrogate model. *IEEE Access* **7**, 77692–77701 (2019).
39. Zhou, Q. *et al.* An active learning radial basis function modeling method based on self-organization maps for simulation-based design problems. *Knowl.-Based Syst.* **131**, 10–27 (2017).
40. Cai, J., King, J., Yu, C., Liu, J. & Sun, L. Support vector regression-based behavioral modeling technique for RF power transistors. *IEEE Microw. Wirel. Comp. Lett.* **28**(5), 428–430 (2018).
41. Jacobs, J. P. Characterization by Gaussian processes of finite substrate size effects on gain patterns of microstrip antennas. *IET Microw. Antennas Propag.* **10**(11), 1189–1195 (2016).
42. Spina, D., Ferranti, F., Antonini, G., Dhaene, T. & Knockaert, L. Efficient variability analysis of electromagnetic systems via polynomial chaos and model order reduction. *IEEE Trans. Comp. Packag. Manuf. Techn.* **4**(6), 1038–1051 (2014).
43. Gu, Q., Wang, Q., Li, X. & Li, X. A surrogate-assisted multi-objective particle swarm optimization of expensive constrained combinatorial optimization problems. *Knowl.-Based Syst.* **223**, 107049 (2021).
44. Zhao, Y., Sun, C., Zeng, J., Tan, Y. & Zhang, G. A surrogate-ensemble assisted expensive many-objective optimization. *Knowl.-Based Syst.* **211**, 106520 (2021).
45. Xiao, S. *et al.* Multi-objective pareto optimization of electromagnetic devices exploiting kriging with lipschitzian optimized expected improvement. *IEEE Trans. Magn.* **54**(3), 1–4 (2018).
46. Koziel, S. & Pietrenko-Dabrowska, A. Expedited feature-based quasi-global optimization of multi-band antennas with Jacobian variability tracking. *IEEE Access* **8**, 83907–83915 (2020).
47. Koziel, S. Fast simulation-driven antenna design using response-feature surrogates. *Int. J. RF Microw. CAE* **25**(5), 394–402 (2015).
48. Pietrenko-Dabrowska, A. & Koziel, S. Fast design closure of compact microwave components by means of feature-based metamodels. *Electronics* **10**, 10 (2021).
49. Zhang, C., Feng, F., Gongal-Reddy, V., Zhang, Q. J. & Bandler, J. W. Cognition-driven formulation of space mapping for equal-ripple optimization of microwave filters. *IEEE Trans. Microw. Theory Technol.* **63**(7), 2154–2165 (2015).
50. Fu, C., Wang, P., Zhao, L. & Wang, X. A distance correlation-based Kriging modeling method for high-dimensional problems. *Knowl.-Based Syst.* **206**, 106356 (2020).
51. Yao, R. *et al.* Deep neural network assisted approach for antenna selection in untrusted relay networks. *IEEE Wirel. Commun. Lett.* **8**(6), 1644–1647 (2019).
52. Xiao, L.-Y., Shao, W., Jin, F.-L., Wang, B.-Z. & Liu, Q. H. Radial basis function neural network with hidden node interconnection scheme for thinned array modeling. *IEEE Antennas Wirel. Propag. Lett.* **19**(12), 2418–2422 (2020).
53. Petrocchi, A. *et al.* Measurement uncertainty propagation in transistor model parameters via polynomial chaos expansion. *IEEE Microw. Wirel. Comp. Lett.* **27**(6), 572–574 (2017).
54. Skaria, S., Al-Hourani, A., Lech, M. & Evans, R. J. Hand-gesture recognition using two-antenna doppler radar with deep convolutional neural networks. *IEEE Sensors J.* **19**(8), 3041–3048 (2019).
55. Prado, D. R., López-Fernández, J. A., Arrebola, M., Pino, M. R. & Goussetis, G. Wideband shaped-beam reflectarray design using support vector regression analysis. *IEEE Antennas Wirel. Propag. Lett.* **18**(11), 2287–2291 (2019).
56. Gorissen, D., Crombecq, K., Couckuyt, I., Dhaene, T. & Demeester, P. A surrogate modeling and adaptive sampling toolbox for computer based design. *J. Mach. Learn. Res.* **11**, 2051–2055 (2010).
57. Marelli, S. and Sudret, B. UQLab: A framework for uncertainty quantification in Matlab. in *2nd International Conference on Vulnerability and Risk Analysis and Management (ICVRAM 2014).* 13–15. 2554–2563 (University of London, 2014).
58. Hu, R., Monebhurrun, V., Himeno, R., Yokota, H. & Costen, F. An adaptive least angle regression method for uncertainty quantification in FDTD computation. *IEEE Trans. Antennas Propag.* **66**(12), 7188–7197 (2018).
59. Yücel, A. C., Bağcı, H. & Michielssen, E. An ME-PC enhanced HDMR method for efficient statistical analysis of multiconductor transmission line networks. *IEEE Trans. Comp. Packag. Manuf. Techn.* **5**(5), 685–696 (2015).
60. Kennedy, M. C. & O'Hagan, A. Predicting the output from complex computer code when fast approximations are available. *Biometrika* **87**, 1–13 (2000).
61. Jacobs, J. P. & Koziel, S. Two-stage framework for efficient Gaussian process modeling of antenna input characteristics. *IEEE Trans. Antennas Propag.* **62**(2), 706–713 (2014).
62. Zhou, Q. *et al.* A sequential multi-fidelity metamodeling approach for data regression. *Knowl.-Based Syst.* **34**, 199–212 (2017).
63. Zhou, Q. *et al.* An active learning metamodeling approach by sequentially exploiting difference information from variable-fidelity models. *Adv. Eng. Inform.* **30**(3), 283–297 (2016).
64. Lin, Q., Zhou, Q., Hu, J., Cheng, Y. & Hu, Z. A sequential sampling approach for multi-fidelity surrogate modeling-based robust design optimization. *ASME. J. Mech. Des.* **144**(11), 111703 (2022).
65. Zhang, L., Wu, Y., Jiang, P., Choi, S. K. & Zhou, Q. A multi-fidelity surrogate modeling approach for incorporating multiple non-hierarchical low-fidelity data. *Adv. Eng. Inform.* **51**, 101430 (2022).
66. Koziel, S. Low-cost data-driven surrogate modeling of antenna structures by constrained sampling. *IEEE Antennas Wirel. Propag. Lett.* **16**, 461–464 (2017).
67. Koziel, S. & Sigurdsson, A. T. Triangulation-based constrained surrogate modeling of antennas. *IEEE Trans. Antennas Propag.* **66**(8), 4170–4179 (2018).
68. Koziel, S. & Pietrenko-Dabrowska, A. Performance-based nested surrogate modeling of antenna input characteristics. *IEEE Trans. Antennas Propag.* **67**(5), 2904–2912 (2019).
69. Koziel, S. & Pietrenko-Dabrowska, A. *Performance-Driven Surrogate Modeling of High-Frequency Structures* (Springer, 2020).
70. Pietrenko-Dabrowska, A. & Koziel, S. Antenna modeling using variable-fidelity EM simulations and constrained co-kriging. *IEEE Access* **8**(1), 91048–91056 (2020).
71. Pietrenko-Dabrowska, A. & Koziel, S. Reliable surrogate modeling of antenna input characteristics by means of domain confinement and principal components. *Electronics* **9**(5), 1–16 (2020).
72. Pietrenko-Dabrowska, A., Koziel, S. & Al-Hasan, M. Cost-efficient bi-layer modeling of antenna input characteristics using gradient kriging surrogates. *IEEE Access* **8**, 140831–140839 (2020).
73. Koziel, S. & Pietrenko-Dabrowska, A. Knowledge-based performance-driven modeling of antenna structures. *Knowl.-Based Syst.* **237**, 107698 (2021).
74. Pietrenko-Dabrowska, A. & Koziel, S. Surrogate modeling of impedance matching transformers by means of variable-fidelity EM simulations and nested co-kriging. *Int. J. RF Microw. CAE* **30**(8), e22268 (2020).

75. Abdullah, M. & Koziel, S. A novel versatile decoupling structure and expedited inverse-model-based re-design procedure for compact single-and dual-band MIMO antennas. *IEEE Access* **9**, 37656–37667 (2021).
76. Koziel, S. & Pietrenko-Dabrowska, A. On computationally-efficient reference design acquisition for reduced-cost constrained modeling and re-design of compact microwave passives. *IEEE Access* **8**, 203317–203330 (2020).
77. Koziel, S. & Pietrenko-Dabrowska, A. Cost-efficient performance-driven modeling of multi-band antennas by variable-fidelity EM simulations and customized space mapping. *Int. J. Numer. Model.* **33**(6), e2778 (2020).
78. Koziel, S. & Ogurtsov, S. *Simulation-Based Optimization of Antenna Arrays* (World Scientific, 2019).
79. Cheng, Q. S., Bandler, J. W. & Koziel, S. Space mapping design framework exploiting tuning elements. *IEEE Trans. Microw. Theory Tech.* **58**(1), 136–144 (2010).
80. Liu, B., Koziel, S. & Zhang, Q. A multi-fidelity surrogate-model-assisted evolutionary algorithm for computationally expensive optimization problems. *J. Comput. Sci.* **12**, 28–37 (2016).
81. Beachkofski, B. & Grandhi, R. Improved distributed hypercube sampling. in *American Institute of Aeronautics and Astronautics Paper AIAA 2002–1274* (2002).
82. Pietrenko-Dabrowska, A. & Koziel, S. On inadequacy of sequential design of experiments for performance-driven surrogate modeling of antenna input characteristics. *IEEE Access* **8**, 78417–78426 (2020).
83. Koziel, S. & Pietrenko-Dabrowska, A. Design-oriented modeling of antenna structures by means of two-level kriging with explicit dimensionality reduction. *AEU Int. J. Electron. Commun.* **127**, 1–12 (2020).
84. Chen, Y.-C., Chen, S.-Y. & Hsu, P. *Dual-Band Slot Dipole Antenna Fed by a Coplanar Waveguide* 3589–3592 (IEEE International Symposium on Antennas and Propagation, 2006).
85. Hua, Z. *et al. A Novel High-Gain Quasi-Yagi Antenna with a Parabolic Reflector* (International Symposium on Antennas and Propagation (ISAP), 2015).
86. Koziel, S. & Pietrenko-Dabrowska, A. Fast and reliable knowledge-based design closure of antennas by means of iterative prediction-correction scheme. *Eng. Comput.* **38**(10), 3710–3731 (2021).

Acknowledgements
The authors would like to thank Dassault Systemes, France, for making CST Microwave Studio available. This work is partially supported by the Icelandic Centre for Research (RANNIS) Grant 217771 and by National Science Centre of Poland Grant 2018/31/B/ST7/02369.

Author contributions
Conceptualization: A.P. and S.K.; Methodology: A.P. and S.K.; Software: A.P., S.K. and L.G.; Validation: A.P. and S.K.; Formal analysis: S.K.; Investigation: A.P. and S.K.; Resources: S.K.; Data curation: A.P., S.K. and L.G.; Writing—original draft preparation: A.P., S.K. and L.G.; Writing—review and editing: A.P. and S.K.; Visualization: A.P., S.K. and L.G.; Supervision: S.K.; Project administration: S.K.; Funding acquisition: S.K. All authors reviewed the manuscript.

Competing interests
The authors declare no competing interests.

Additional information
Correspondence and requests for materials should be addressed to A.P.-D.

Reprints and permissions information is available at www.nature.com/reprints.

Publisher's note Springer Nature remains neutral with regard to jurisdictional claims in published maps and institutional affiliations.

Open Access This article is licensed under a Creative Commons Attribution 4.0 International License, which permits use, sharing, adaptation, distribution and reproduction in any medium or format, as long as you give appropriate credit to the original author(s) and the source, provide a link to the Creative Commons licence, and indicate if changes were made. The images or other third party material in this article are included in the article's Creative Commons licence, unless indicated otherwise in a credit line to the material. If material is not included in the article's Creative Commons licence and your intended use is not permitted by statutory regulation or exceeds the permitted use, you will need to obtain permission directly from the copyright holder. To view a copy of this licence, visit http://creativecommons.org/licenses/by/4.0/.

© The Author(s) 2022

MOST WIEDZY Downloaded from mostwiedzy.pl